Universal responses in nonmagnetic polar metals

Fabian Jäger ⬡, Nicola A. Spaldin, and Sayantika Bhowal ⬡*
Materials Theory, ETH Zurich, Wolfgang-Pauli-Strasse 27, 8093 Zurich, Switzerland

We demonstrate that two phenomena, the kinetic magnetoelectric effect and the nonlinear Hall effect, are universal to polar metals as a consequence of their coexisting and contraindicated polarization and metallicity. We show that measurement of the effects provides a complete characterization of the nature of the polar metal, in that the nonzero response components indicate the direction of the polar axis, and the coefficients change signs on polarization reversal and become zero in the nonpolar phase. We illustrate our findings for the case of electron-doped $PbTiO_3$ using a combination of density functional theory and model Hamiltonian-based calculations. Our model Hamiltonian analysis provides crucial insight into the microscopic origin of the effects, showing that they originate from inversion-symmetry-breaking-induced interorbital hoppings that correlate to an asymmetric charge density quantified by odd-parity charge multipoles. Our paper both heightens the relevance of the kinetic magnetoelectric and nonlinear Hall effects, and broadens the platform for investigating and detecting odd-parity charge multipoles in polar metals.

I. INTRODUCTION

Anderson and Blount challenged the conventional notion that electric polarization is screened by itinerant carriers in their proposal [1], advocating instead for its combination with metallicity. This proposition, once deemed unlikely, has now been substantiated by the recent practical materialization of polar metals [2–4]. These have consequently opened a paradigm for investigating numerous intriguing physical effects that result from the coexistence of the seemingly mutually exclusive properties of polarity and metallicity [5–8].

In the present paper, we point out two such effects, the kinetic magnetoelectric effect (KME) and nonlinear Hall effect (NHE), which are universal to all polar metals. While these effects have been sporadically investigated in some candidate polar metal systems [9–11], a consensus in applying these effects to characterizing polar metals is still missing. Here we show that both effects simultaneously carry key signatures of the polar metal phase, that is, the direction of the polar axis, the switchability of the polarization, and the ferroelectriclike nonpolar to polar structural transition, and so provide a complete characterization of polar metals. Furthermore, we reveal the microscopic origin of these two effects by analyzing asymmetries in the charge density. While both effects are dominated by contributions from the electric dipole

moment, i.e., the first-order asymmetry in the charge density, the electric octupole moment, characterizing the third-order asymmetry in the charge density, also plays an important role.

The KME is a linear effect, describing electric field ($\mathcal{E}$) induced magnetization $\mathcal{M}_j = \mathcal{K}_{ij}\mathcal{E}_i$ in a nonmagnetic metal [12–16]. Here $\mathcal{K}_{ij}$ is KME response. Unlike the conventional magnetoelectric effect observed in time-reversal broken insulators [17], the KME is a current-induced effect that can occur in nonmagnetic metals that preserve time-reversal symmetry. Although known for over three decades [12], recent advances in topological Weyl semimetals [18,19] and the elucidation of the symmetry requirements [14,16] have reignited interest in this effect.

The magnetization that results from the current flow in the KME further gives rise to a transverse Hall current (J) as a second-order response to the applied electric field, $J_i = \chi_{ijk}\mathcal{E}_j\mathcal{E}_k$, known as a NHE [20]. Here, χ_{ijk} represents the nonlinear Hall conductivity (NHC) tensor, with i, j, k denoting the Cartesian directions. Investigation of NHC in nonmagnetic metals is particularly intriguing due to the absence of the linear anomalous Hall effect in the presence of time-reversal symmetry. The effect has been extensively studied in various materials, including Weyl semimetals [21] and van der Waals metals such as WTe_2 [9,10], strained MoS_2 [22], and twisted bilayer WSe_2 [23]. Materials featuring tunable NHC hold significant promise for a wide range of technological applications, including efficient energy harvesting, infrared detectors, and next-generation wireless techniques, all of which leverage second-harmonic generation or rectification [24–26].

Within the relaxation-time approximation for the nonequilibrium electron distribution, both KME and NHC responses can be elegantly recast in terms of the reduced KME response $\tilde{\mathcal{K}}_{ij}$, dictated by the equilibrium reciprocal-space magnetic (spin plus orbital) moment $\vec{m}(\vec{k})$, and the Berry curvature

---

*Present address: Department of Physics, Indian Institute of Technology Bombay, Mumbai 400076, India; sbhowal@iitb.ac.in

dipole (BCD) $\mathcal{D}_{ij}$, respectively [14,16,20],

$$\mathcal{K}_{ij} = \frac{e\tau}{\hbar}\tilde{\mathcal{K}}_{ij},$$

$$\chi_{ijk} = -\varepsilon_{ilk}\frac{e^3\tau}{2(1+i\omega\tau)}\mathcal{D}_{jl}. \qquad (1)$$

Here τ and ε_{ijk} are, respectively, the relaxation time constant and the Levi-Civita symbol. Both the reduced KME response $\tilde{\mathcal{K}}_{ij}$ and the BCD are intrinsic properties of a material and are given by [9,10,14,16]

$$\tilde{\mathcal{K}}_{ij} = -\sum_n \frac{1}{(2\pi)^3}\int d^3k\, m_j^n(\vec{k})\partial_{k_i}\epsilon_k^n\left(\frac{\partial f_0}{\partial\epsilon_k^n}\right)$$

$$= \sum_n \frac{1}{(2\pi)^3}\int d^3k\,\left(\partial_{k_i}m_j^n\right)f_0 \qquad (2)$$

and

$$\mathcal{D}_{ij} = -\sum_n \frac{1}{(2\pi)^3}\int d^3k\,\Omega_j^n(\vec{k})\partial_{k_i}\epsilon_k\left(\frac{\partial f_0}{\partial\epsilon_k^n}\right)$$

$$= \sum_n \frac{1}{(2\pi)^3}\int d^3k\,\left(\partial_{k_i}\Omega_j^n\right)f_0. \qquad (3)$$

Here e, n, f_0, and $\vec{\Omega}$ are the electronic charge, band index, equilibrium Fermi distribution function, and Berry curvature, respectively. Both $\tilde{\mathcal{K}}_{ij}$ and $\mathcal{D}_{ij}$ are allowed in nonmagnetic metals with gyrotropic point group symmetry [9,10,14,16]. Since all polar point groups are gyrotropic [27,28], both KME and NHE are allowed by symmetry in all polar metals.

Interestingly, the components of the reciprocal-space magnetic moment $\vec{m}(\vec{k})$, which contributes to the KME response, is determined by the direction of the electric polarization [29]. Similarly, the antisymmetric component of the BCD, $\mathcal{D}^- = (\mathcal{D} - \mathcal{D}^T)/2$, correlates with the orientation of the polar axis $\vec{d}$, $d_i \equiv \varepsilon_{ijk}\mathcal{D}_{jk}^-/2$ [20], suggesting a possible switching of both responses for a switchable orientation of the polar distortion. Furthermore, since both effects are forbidden by symmetry in an inversion symmetric structure, a structural transition from a centrosymmetric to a noncentrosymmetric polar structure can be inferred from the onset of these effects as the temperature is lowered.

We illustrate these concepts by explicitly considering the case of electron-doped $PbTiO_3$ (PTO) as an example material. Undoped PTO is a prototypical conventional ferroelectric insulator [30]. Interestingly, even upon electron doping via replacing the Ti^{4+} ions by Nb^{5+} ions, the resulting $PbTi_{1-x}Nb_xO_3$ was observed to sustain the electric polarization up to $x = 0.12$, at which point the system also becomes conducting [31,32]. In the present paper, using both first-principles density functional theory (DFT) and a model Hamiltonian-based approach we show that the presence as well as the orientation of the polar axis in the polar metal phase of doped PTO can be determined from the nonzero components of KME and the NHE.

The remainder of this paper is organized as follows. We start by describing the computational details in Sec. II. This is followed by the results and discussions in Sec. III, where we present our computational results for doped PTO, describing the existence and tuning of KME and NHE, the effect of spin-

orbit coupling (SOC), the momentum space distribution of the orbital moment and Berry curvature that determine these effects, their microscopic origin within the model Hamiltonian framework, and the role of odd-parity charge multipoles. Finally, we summarize our results in Sec. IV and give a proposal for measuring these effects.

II. COMPUTATIONAL DETAILS

The responses $\tilde{\mathcal{K}}_{ij}$ and $\mathcal{D}_{ij}$ are computed using the QUANTUM ESPRESSO [33] and WANNIER90 codes [34–36]. We use fully relativistic norm-conserving pseudopotentials for all the atoms with the following valence electron configurations: Pb ($6s^26p^2$), Ti ($4s^23d^2$), and O ($2s^22p^4$). Self-consistency is achieved with a $12 \times 12 \times 10$ k-point mesh and a convergence threshold of 10^{-7} Ry. The *ab initio* wave functions, thus obtained, are then projected to maximally localized Wannier functions [34,35] using the WANNIER90 code [36]. In the disentanglement process, as initial projections, we choose 42 Wannier functions per unit cell which include the s and p orbitals of Pb, d orbitals of Ti, and s and p orbitals of O atoms, excluding the rest. After the disentanglement is achieved, the Wannierization process is converged to 10^{-10} Å^2. We then compute the k-space distribution of the orbital moment and the Berry curvature as well as the reduced KME response, $\tilde{\mathcal{K}}_{ij}$, and the BCD $\mathcal{D}_{ij}$ for a $150 \times 150 \times 140$ k-point mesh. To estimate the doped charge density, we also compute the density of states (DOS) for the same k-point mesh.

III. RESULTS AND DISCUSSION

A. NHE and KME and their tuning in polar metals

We start with the electronic structure of PTO, which crystallizes in the noncentrosymmetric tetragonal ($P4mm$) structure with the polar C_{4v} point group symmetry [30]. In tetragonal PTO, both Pb^{2+} ($6s^2$ lone pair) and Ti^{4+} ($3d^0$) ions off-center with respect to the surrounding O^{2-} ions, resulting in a net polarization along $\hat{z}$, which is switchable to $-\hat{z}$ using an external electric field. We refer to these two structures, schematically depicted in Fig. 1(a), as $+P$ and $-P$, respectively. The electronic structure of the polar undoped PTO (corresponding to $+P$) is shown in Fig. 1(b), depicting the insulating band structure in which the occupied O-p states and the formally empty Ti-t_{2g} states form the valence band maximum and conduction band minimum (CBM), respectively.

The doping electrons in doped PTO occupy the CBM, leading to a metallic band structure within the rigid band approximation. To compute $\tilde{\mathcal{K}}_{ij}$ and $\mathcal{D}_{ij}$, we first project the computed *ab initio* wave functions onto maximally localized Wannier functions and then disentangle the relevant bands (see Sec. II for computational details) from the rest using the WANNIER90 code [36]. As depicted in Fig. 1(b), the Wannierised bands agree well with the full DFT band structure. The central quantities $\tilde{\mathcal{K}}_{ij}$ and $\mathcal{D}_{ij}$ in determining the magnitudes of the KME and NHE are then computed using the first expressions in Eqs. (2) and (3), respectively, as implemented within the WANNIER90 code [34–36].

The computed nonzero components of the reduced KME response, $\tilde{\mathcal{K}}_{xy}$ (blue circle), $\tilde{\mathcal{K}}_{yx}$ (red circle), and BCD $\mathcal{D}_{xy}$ (blue circle) and $\mathcal{D}_{yx}$ (red circle) are shown as functions of
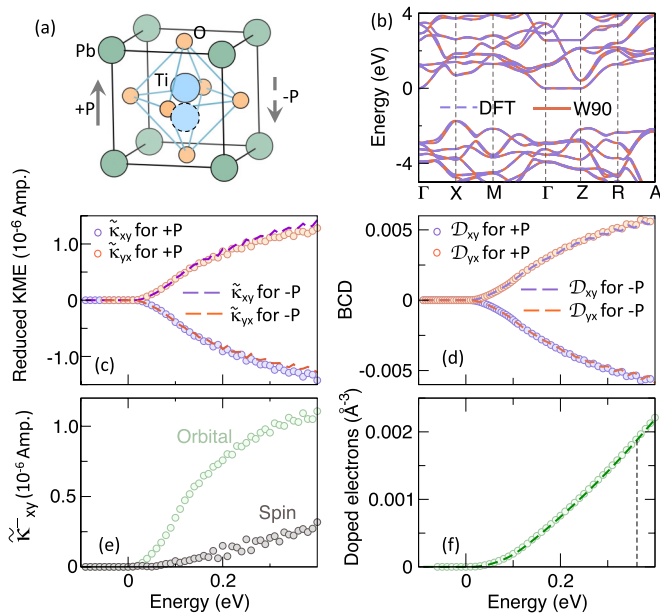
FIG. 1. (a) Schematic illustration of the crystal structure of PTO, showing the off-centering of the Ti atom leading to a polarization $+P$ along $\hat{z}$. The dashed circle indicates the displacement of the Ti atom in the opposite direction, switching the direction of the polarization ($-P$) indicated by the dashed arrow. (b) Comparison of the band structure of undoped PTO, computed within DFT (dashed line) and that obtained from WANNIER90 (solid line), showing good agreement between the two. (c) Computed reduced KME response components $\tilde{\mathcal{K}}_{xy}$ (blue) and $\tilde{\mathcal{K}}_{yx}$ (red) for the two directions of polarization $+P$ (circle) and $-P$ (dashed line), shown in (a), as a function of energy. (d) BCD components $\mathcal{D}_{xy}$ (blue) and $\mathcal{D}_{yx}$ (red) for the polarization directions, $+P$ (circles) and $-P$ (dashed line) as a function of energy. (e) Energy variation of the spin and orbital contributions to the absolute value of the antisymmetric component of the reduced KME response, $\tilde{\mathcal{K}}_{xy}^{-} = \frac{1}{2}(\tilde{\mathcal{K}}_{xy} - \tilde{\mathcal{K}}_{yx})$ for polarization $+P$. (f) Energy variation of the doped electron densities for the two polarization directions, $+P$ (circles) and $-P$ (dashed line). The vertical black dashed line corresponds to the experimentally achieved maximum doped electron density, that maintains the polarity of the structure. The zero of energy in [(b)–(f)] refers to the CBM of undoped PTO.

energy in Figs. 1(c) and 1(d) for the $+P$ structure. To determine whether the energy range used in the computation is experimentally achievable, we further compute the doped electron density by integrating the corresponding DOS and show the results in Fig. 1(f). Note that the zero of the energy corresponds to the CBM for the undoped case. The vertical dashed line in Fig. 1(f) indicates the maximum doped electron density up to which the polarity of the lattice persists in the experiments [31,32], justifying the chosen energy range.

We note from Figs. 1(c) and 1(d) that $\tilde{\mathcal{K}}_{xy} = -\tilde{\mathcal{K}}_{yx}$ and $\mathcal{D}_{xy} = -\mathcal{D}_{yx}$, consistent with the C_{4v} point group symmetry. Here $\tilde{\mathcal{K}}_{ij}$ has both spin and orbital contributions. To understand the relative contributions of the two, the individual spin and orbital contributions are also shown in Fig. 1(e) for the absolute value of the antisymmetric component of the reduced KME response, $\tilde{\mathcal{K}}_{xy}^{-} = \frac{1}{2}(\tilde{\mathcal{K}}_{xy} - \tilde{\mathcal{K}}_{yx})$. This clearly shows that the orbital contribution dominates over the spin contribution. Such a current-induced orbital magnetization has also been
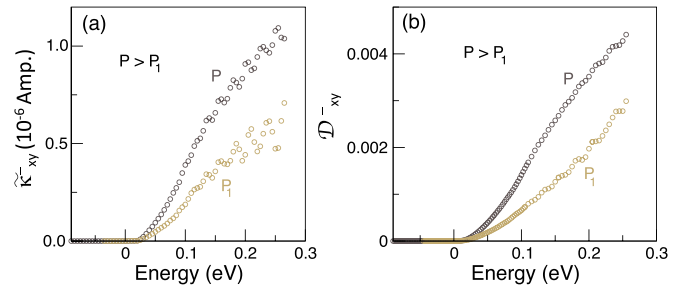

FIG. 2. (a) Comparison of the energy variation of the absolute value of $\tilde{\mathcal{K}}_{xy}^{-}$ for two different displacements of the Ti ion, P and P_1, with the former being larger than the latter. (b) Comparison of the energy variation of the absolute value of the antisymmetric BCD component $\mathcal{D}_{xy}^{-} = \frac{1}{2}(\mathcal{D}_{xy} - \mathcal{D}_{yx})$ for the same P and P_1.

reported for other systems with broken inversion symmetry [13,37–39] and may have important implications in the field of orbitronics.

To see the effect of the polarization direction, we reverse the direction of the displacement of the ions, leading to the $-P$ structure [see Fig. 1(a)]. The corresponding computed $\tilde{\mathcal{K}}_{xy}$ (blue dashed line), $\tilde{\mathcal{K}}_{yx}$ (red dashed line), and $\mathcal{D}_{xy}$ (blue dashed line), $\mathcal{D}_{yx}$ (red dashed line) are shown in Figs. 1(c) and 1(d), respectively. We note that in this case, all the computed quantities switch sign compared to the $+P$ structure, while still maintaining the symmetry of the C_{4v} point group, as discussed above.

We further artificially decrease the amount of the Ti displacement to see the effect of the magnitude of polarization. We refer to the corresponding structure as $+P_1$. The computed absolute values of $\tilde{\mathcal{K}}_{xy}^{-}$ and $\mathcal{D}_{xy}^{-} = \frac{1}{2}(\mathcal{D}_{xy} - \mathcal{D}_{yx})$ for $+P_1$ are depicted in Figs. 2(a) and 2(b) respectively, together with the values for $+P$. We find that both $\tilde{\mathcal{K}}_{xy}^{-}$ and $\mathcal{D}_{xy}^{-}$ have smaller magnitudes for $+P_1$ compared to $+P$, suggesting that both effects not only depend on the direction of polarization but also on the magnitude of the polarization.

It is important to point out here that polarization is not the only factor that contributes to the value of the responses. For example, both responses also depend on the details of the electronic structure [see Eqs. (2) and (3)]. As a result, the situation can be more complicated if there is a drastic change in the band structure with the change in electric polarization. Nevertheless, our analysis clearly shows that the polarization is an important factor and that both KME and NHE are tunable by changing the direction or magnitude of the electric polarization.

B. Effect of spin-orbit coupling

To understand the dependence on SOC, we perform additional calculations with the SOC turned off in our computations. Comparisons of the computed $\tilde{\mathcal{K}}_{xy}^{-}$ and $\mathcal{D}_{xy}^{-}$ both in the absence and presence of SOC are shown in Figs. 3(a) and 3(b). As seen from these figures, both $\tilde{\mathcal{K}}_{xy}^{-}$ and $\mathcal{D}_{xy}^{-}$ exist even without the SOC. This suggests that both effects occur due to the symmetry of the structure and the presence of SOC is not necessary. Indeed, in the absence of SOC, the KME response is driven by the orbital contribution. With the
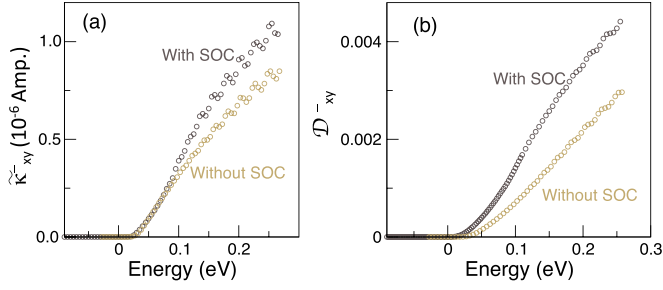
FIG. 3. Comparison of the energy variation of the absolute value of (a) $\tilde{\mathcal{K}}_{xy}^-$ and (b) $\mathcal{D}_{xy}^-$ in the absence and presence of SOC.

inclusion of SOC, the orbital degrees of freedom couple to the spin degrees of freedom, leading to additional current-induced spin magnetization in the system. We notice that, while the inclusion of SOC increases the magnitudes of both effects, the change in the KME response is smaller than that of the NHC. This can be attributed to the weak SOC-induced spin contribution to the KME response as depicted in Fig. 1(e).

To gain further insight into the effect of SOC, we analyzed the corresponding band structures. Figures 4(a) and 4(c) depict the conduction bands of undoped PTO both in the absence and presence of spin-orbit interaction. These bands have dominating contributions coming from Ti-d orbitals [see Fig. 4(b)]. A striking feature of the band structure in the presence of SOC is the lifting of the degeneracy of the bands with opposite spin polarization. In particular, the spin-polarization direction of the bands is normal to the momentum direction. For example, as shown in Fig. 4(c), the bands along the k_x
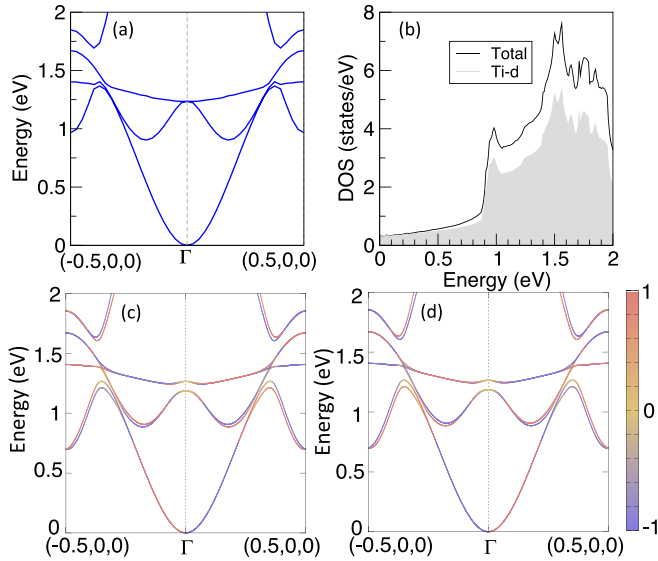

FIG. 4. Effect of spin-orbit coupling on the band structure. (a) Conduction bands of undoped PTO in the absence of SOC. (b) The corresponding total densities of states (DOS) and partial Ti-d DOS, showing the dominance of the Ti-d states in the CBM. The band structures in the presence of spin-orbit interaction for (c) $+P$ and (d) $-P$ electric polarization directions [see Fig. 1(a)]. The color map represents the S_y spin polarization of the bands. Zero of energy corresponds to the CBM.

direction are S_y spin polarized. Similarly, the bands are S_x spin polarized along the k_y direction in momentum space (not shown here). The energy splitting of the spin-polarized bands is, however, weak near the CBM, justifying the small spin contribution to the KME response and, consequently, the weak changes in the KME response upon inclusion of SOC effects.

We note that the spin splitting $\Delta\varepsilon_s(\vec{k})$ reverses as the momentum direction is reversed, i.e., it is antisymmetric in $\vec{k}$, corresponding to p-wave symmetry. This is due to the presence of time-reversal symmetry, which dictates $\Delta\varepsilon_s(\vec{k}) = \varepsilon_\uparrow(\vec{k}) - \varepsilon_\downarrow(\vec{k}) = -\Delta\varepsilon_s(-\vec{k})$. Such antisymmetric, spin-orbit-induced spin splitting is known as the Rashba effect [40]. Interestingly, as shown in Fig. 4(d), for the opposite electric polarization direction in the $-P$ structure, the spin polarization of the bands is also reversed. Such spin-orbit-induced spin splitting and its reversal upon switching the electric polarization could be observed using techniques like magnetic Compton scattering [29], which probes the spin-polarized electron momentum density in materials.

The switching of the spin polarization on electric polarization reversal explains the reversal of the spin contribution to the KME response for the $-P$ structure. Both the KME and the NHC responses are, however, significant in magnitude even without the SOC. Hence, further understanding of the two responses requires analysis of the orbital moment and Berry curvature in reciprocal space, which are present even without SOC. We discuss these below.

C. *k*-space distribution of orbital moment and Berry curvature

We now analyze the k-space distributions of the relevant x and y components of the orbital magnetic moment and Berry curvature in the k_x-k_y plane. Since the $\tilde{\mathcal{K}}_{ij}$ response is dominated by the orbital contribution, here for simplicity we only consider the orbital magnetic moment distribution. The k-resolved contribution to the orbital magnetization at equilibrium, $\vec{\mathcal{M}}^{\mathrm{orb}}(\vec{k})$, is computed within the modern theory of orbital magnetization [41–44] as implemented in the WANNIER90 code [45]:

$$\vec{\mathcal{M}}^{\mathrm{orb}}(\vec{k}) = \sum_n \left[\frac{e}{2\hbar}\mathrm{Im}\langle\boldsymbol{\nabla}_k u_k^n| \times \left[\mathcal{H}(\vec{k}) - \epsilon_k^n\right]|\boldsymbol{\nabla}_k u_k^n\rangle \right.$$
$$\left. + \frac{e}{\hbar}\mathrm{Im}\langle\boldsymbol{\nabla}_k u_k^n| \times \left[\epsilon_k^n - \epsilon_{\mathrm{F}}\right]|\boldsymbol{\nabla}_k u_k^n\rangle \right]. \quad (4)$$

Here, ϵ_k^n and u_k^n are the energy eigenvalues and eigenfunctions of the Hamiltonian $\mathcal{H}(\vec{k})$ obtained from Wannierization, ϵ_{F} is the Fermi energy, and the sum is over all occupied bands n. The computed value of $\mathcal{M}_x^{\mathrm{orb}}$ ($\mathcal{M}_y^{\mathrm{orb}}$) is shown in Fig. 5(a) (Fig. 8 in Appendix 1).

We note that the second term in Eq. (4) does not contribute to the KME response (see Appendix 2 for details) and, hence, only the first term is relevant to us. The first term in Eq. (4) represents the intrinsic Bloch orbital moment $\vec{m}_n^{\mathrm{orb}}(\vec{k})$ [41,46] that also appears in the expression for reduced KME response in Eq. (2).
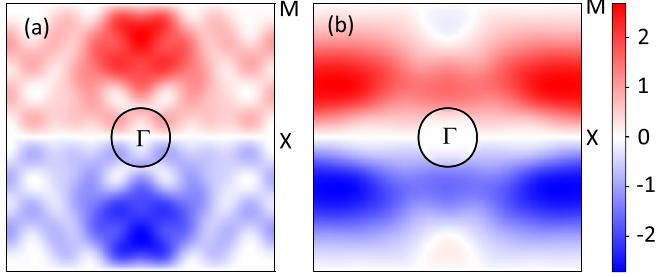
FIG. 5. Computed k-space distributions of (a) $\mathcal{M}_x^{\mathrm{orb}}$ (in units of eV/Å^2) and (b) the Berry curvature Ω_x (in units of Å^2) in PTO for the doped electron density ~ 0.001Å^{-3}, corresponding to ~ 0.202 eV above the CBM of undoped PTO. The black circle around the Γ point indicates the Fermi surface corresponding to this electron density. $\vec{\mathcal{M}}^{\mathrm{orb}}(\vec{k})$ and $\vec{\Omega}(\vec{k})$ (summed over occupied bands n) are computed using Eqs. (4) and (5). The high-symmetry k points are indicated on the $k_z = 0$ plane for easy reference.

The k-space distribution of the Berry curvature is computed using the Kubo formula [47],

$$\Omega_k^n(\vec{k}) = -2\hbar^2 \sum_{m \neq n} \mathrm{Im} \frac{\langle u_k^n | v_i | u_k^m \rangle \langle u_k^m | v_j | u_k^n \rangle}{(\epsilon_k^n - \epsilon_k^m)^2}, \qquad (5)$$

where $\vec{v} = \frac{1}{\hbar} \frac{\partial \mathcal{H}}{\partial \vec{k}}$ is the velocity operator and (i, j, k) are cyclic permutations of the Cartesian directions (x, y, z). The computed value of the Berry curvature component $\Omega_x^n(\vec{k})$ ($\Omega_y^n(\vec{k})$) is shown in Fig. 5(b) (Fig. 8 in Appendix 1).

The computed k-space distributions of $\vec{\mathcal{M}}^{\mathrm{orb}}(\vec{k})$ and $\vec{\Omega}(\vec{k})$ can be understood based on the symmetries of the crystal structure and are detailed in Appendix 2. The existence of these two quantities in different parts of the BZ of PTO, even though their BZ sum is zero due to the presence of $\mathcal{T}$ symmetry at equilibrium, explains the current induced magnetization in the KME response and, consequently, the NHC. It is important to point out that both $\vec{\mathcal{M}}^{\mathrm{orb}}(\vec{k})$ and $\vec{\Omega}(\vec{k})$ exist even in the absence of SOC, justifying the existence of the two responses even without the SOC. We also notice an interesting resemblance between the computed orbital texture and the spin polarization of the Rashba-split bands in Sec. III B, with both having the same toroidal distribution in momentum space.

D. Microscopic origin: role of odd-parity charge multipoles

1. Model Hamiltonian

To understand the microscopic origin of the k-space orbital texture and Berry curvature, and, hence, the two responses, we construct a minimal tight-binding (TB) model in the basis set of the Ti-t_{2g} orbitals, $\{d_{xy}, d_{yz}, d_{xz}\}$. For small doping, the doped electrons occupy the Ti-d bands [see Fig. 4(b)] around the Γ point of the BZ that correspond to the CBM for the undoped case, indicated by the black circles in Fig. 5. We, therefore, expand the TB model around the Γ point, and the resulting low energy model Hamiltonian is given by

$$\mathcal{H}(\vec{k}) = \mathcal{H}_{\mathrm{inv}}(\vec{k}) + \mathcal{H}_{\mathrm{BI}}(\vec{k}). \qquad (6)$$

TABLE I. Effective hopping parameters (in units of 10^{-2} Ry) in Eq. (8), derived from the computed TB hopping parameters and on-site energies for PTO using the NMTO downfolding technique.

t_{eff}^1	t_{eff}^2	t_{eff}^3	t_{eff}^4	t_{eff}^5	t_{eff}^6	t_{eff}^7	t_{eff}^8	t_{eff}^9
4.95	−2.26	0.4	10.09	−0.19	−0.97	−1.59	−0.48	−0.28

Here $\mathcal{H}_{\mathrm{inv}}$ is the inversion symmetric part of the Hamiltonian and is given by

$$\mathcal{H}_{\mathrm{inv}} = \begin{pmatrix} h_{11} & h_{12} & h_{13} \\ h_{12} & h_{22} & h_{23} \\ h_{13} & h_{23} & h_{33} \end{pmatrix}, \qquad (7)$$

with the explicit analytical forms of the elements h_{ij} up to quadratic order in k given below:

$$\begin{aligned}
h_{11} &= t_{\mathrm{eff}}^1 - t_{\mathrm{eff}}^2 (k_x^2 + k_y^2) a^2 - t_{\mathrm{eff}}^3 k_z^2 c^2, \\
h_{22} &= t_{\mathrm{eff}}^4 - t_{\mathrm{eff}}^5 k_x^2 a^2 - t_{\mathrm{eff}}^6 k_y^2 a^2 - t_{\mathrm{eff}}^7 k_z^2 c^2, \\
h_{33} &= t_{\mathrm{eff}}^4 - t_{\mathrm{eff}}^6 k_x^2 a^2 - t_{\mathrm{eff}}^5 k_y^2 a^2 - t_{\mathrm{eff}}^7 k_z^2 c^2, \\
h_{12} &= t_{\mathrm{eff}}^8 k_x k_z ac, \\
h_{13} &= t_{\mathrm{eff}}^8 k_y k_z ac, \\
h_{23} &= t_{\mathrm{eff}}^9 k_x k_y a^2.
\end{aligned} \qquad (8)$$

Here a and c are the lattice constants for the tetragonal unit cell. Note that since $\mathcal{H}_{\mathrm{inv}}$ is inversion symmetric, it contains only terms that are even in k. The effective hopping parameters t_{eff}^i, $i = 1, 9$ are linear combinations of the different effective t_{2g}-t_{2g} electronic hopping parameters that we extract using the N$^{\mathrm{th}}$ order muffin-tin orbital (NMTO) downfolding technique [48]. The computed parameters for one direction of polarization $(+P)$ are listed in Table I. We consider up to fourth-nearest neighbor (NN) interactions. It is important to consider such long-range neighbor interactions which are needed to capture the physics of the two effects of interest, as we discuss later.

On the other hand, $\mathcal{H}_{\mathrm{BI}}$ includes the hopping parameters that are induced by the broken $\mathcal{I}$ symmetry. It can be written in terms of the components of the orbital angular momentum operator $\hat{\vec{L}}$:

$$\begin{aligned}
\mathcal{H}_{\mathrm{BI}} &= \frac{\alpha a}{\hbar} (k_x \hat{L}_y - k_y \hat{L}_x) - \frac{\alpha a^3}{6\hbar} (k_x^3 \hat{L}_y - k_y^3 \hat{L}_x) \\
&\quad - \frac{\beta ac^2}{\hbar} k_z^2 (k_x \hat{L}_y - k_y \hat{L}_x) - \frac{\gamma a^3}{\hbar} k_x k_y (k_y \hat{L}_y - k_x \hat{L}_x).
\end{aligned} \qquad (9)$$

The parameters α, β, γ are determined by the broken $\mathcal{I}$-symmetry-induced hopping parameters and have opposite signs for $+P$ and $-P$. In centrosymmetric PTO, α, β, γ are zero, so $\mathcal{H} = \mathcal{H}_{\mathrm{inv}}$. In addition, $t_{\mathrm{eff}}^8 = -2(t^x - t^y) = 0$ in the centrosymmetric structure, where t^x and t^y are the fourth-NN interorbital hopping integrals, which we discuss in detail later. The components of the orbital angular momentum operator in
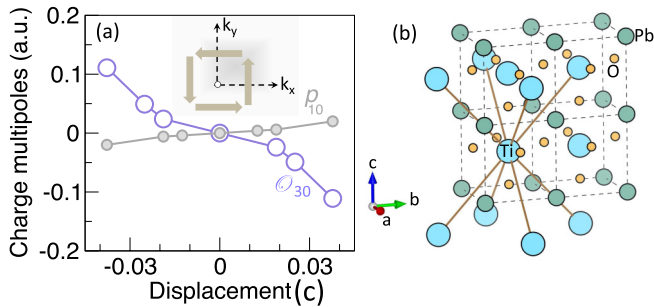
FIG. 6. Atomic-site charge dipole moment component p_{10} and octupole moment component $\mathcal{O}_{30}$ on the Ti^{4+} ions as a function of the displacement (in units of out-of-plane lattice constant c) of the Ti ion from the center of the unit cell in PTO. The inset shows the schematic for the toroidal arrangement of the orbital (spin) moment (indicated in thick arrows) in the k_x-k_y plane due to the first term in the Hamiltonian (9) driven by the charge dipole. (b) Fourth-nearest neighbor Ti atoms (connected by the brown straight lines) along $(\pm a, 0, \pm c)$ and $(0, \pm a, \pm c)$. Note that in the cubic high-symmetry structure with $c = a$, these are second-nearest neighbors.

Eq. (9) in the t_{2g} orbital basis $\{d_{xy}, d_{yz}, d_{xz}\}$ are given by

$$L_x^{(t_{2g})} = \hbar \begin{pmatrix} 0 & 0 & -i \\ 0 & 0 & 0 \\ i & 0 & 0 \end{pmatrix}, \quad L_y^{(t_{2g})} = \hbar \begin{pmatrix} 0 & i & 0 \\ -i & 0 & 0 \\ 0 & 0 & 0 \end{pmatrix},$$

$$L_z^{(t_{2g})} = \hbar \begin{pmatrix} 0 & 0 & 0 \\ 0 & 0 & i \\ 0 & -i & 0 \end{pmatrix}. \tag{10}$$

It is important to point out here that, although the considered model Hamiltonian is specific to PTO, the inversion symmetry breaking in any polar metal system will always induce new channels for interorbital hopping that are otherwise forbidden in an inversion symmetric structure (e.g., in the high-temperature nonpolar phase). This is independent of the choice of orbitals as the basis of the model Hamiltonian. For example, the inclusion of all Ti-d orbitals in the model or O-p orbitals in addition to the Ti-d orbitals will not affect this conclusion.

The advantage of writing $\mathcal{H}_{BI}$ in terms of the $\hat{\vec{L}}$ operators is that we can readily identify the resulting orbital texture in momentum space. For example, the first term in Eq. (9), which is linear in $\vec{k}$, depicts a toroidal arrangement of orbital magnetic moment in reciprocal space [see the inset of Fig. 6(a)]. Such a toroidal arrangement of the orbital moment in k space is also in agreement with our DFT results (see Figs. 5 and 8) and the symmetry analysis presented in Appendix 1. We note that the first term in Eq. (9) has a form $\sim(\vec{k} \times \vec{L})$, which is an orbital counterpart of the (spin) Rashba effect $\sim(\vec{k} \times \vec{\sigma})$ and, hence, is often referred to as an orbital Rashba effect [49,50].

We note that formation of the orbital moment in the BZ of the material is related to the interorbital hopping, as discussed before. The hybridization between different orbitals, mediated by these hopping parameters, gives rise to complex orbitals in momentum space that carry a net orbital moment, as also represented by the Hamiltonian in Eq. (9). Since interorbital hopping is always present in polar metal systems, the momentum space Rashba-like orbital texture is also general to

all polar metals, with the specific component of the orbital moment determined by the polar axis of the material. This further suggests the polar metals as potential candidates for orbitronic applications, in which the momentum space orbital texture is an important ingredient.

In the presence of SOC, the orbital texture in the orbital Rashba effect couples to the spin, additionally leading to spin texture and the Rashba effect in PTO [51] as also found in our DFT calculations (see Sec. III B). Here, for simplicity, we do not include SOC in our model Hamiltonian in Eq. (6), since both KME and BCD exist even in its absence (see Fig. 3).

2. Role of odd-parity charge multipoles

Interestingly, each term of different order in $\vec{k}$ in the Hamiltonian $\mathcal{H}_{BI}$ of Eq. (9) has a direct correlation to a corresponding odd-parity charge multipole. Recently, we showed that the k-space orbital and spin textures in ferroelectrics result from the k-space magnetoelectric multipoles that are reciprocal to the real-space odd-parity charge multipoles [29]. The odd-parity charge multipoles characterize the asymmetries in the charge density that are present due to the broken $\mathcal{I}$ symmetry. For example, the electric dipole dictates the first-order asymmetry in the charge density, while the electric octupole corresponds to the third-order asymmetry, and so on. The first term within the parentheses in Eq. (9), which is linear in $\vec{k}$, corresponds to the k-space representation of the electric dipole moment (p_{10}) whereas the remaining terms, which are all cubic in $\vec{k}$, correspond to the electric octupole moment ($\mathcal{O}_{30}$).

To verify the existence of the local electric dipoles and octupoles in PTO, we decompose the $\mathcal{T}$ symmetric density matrix $\rho_{lm,l'm'}$, computed within the DFT framework, into parity-odd tensor moments and explicitly compute the atomic-site electric dipole and octupole moments, for which only the odd $l - l'$ terms contribute [52]. The computed odd-parity charge multipoles on the Ti^{4+} ions are non-zero in the polar structure, as shown in Fig. 6(a), and confirm the presence of a ferrotype ordering of electric dipole component p_{10} and octupole component $\mathcal{O}_{30}$ at the Ti site. Here the indices at the suffix of the multipole components represent the l and m indices of the spherical harmonics that are used to build these charge multipoles. The electric dipole moment $\vec{p}$ is a tensor of rank 1 (vector), with p_{10} indicating its z component. Similarly, the octupole moment $\mathcal{O}_{ijk}$ is a totally symmetric tensor of rank 3 with seven components. The $\mathcal{O}_{30}$ component has the representation $\frac{1}{2}z(5z^2 - r^2)$.

Correlating each of the terms in the Hamiltonian (9) to odd-parity charge multipoles of different orders provides the multipolar description of the two responses in polar metals. This opens up a door for investigating as well as detecting the higher-order multipoles in polar metals. Furthermore, this confirms that for any polar metals with nonzero charge dipoles and octupoles due to broken mirror symmetry, analogous terms to those in the Hamiltonian (9) will emerge, with their explicit form depending on which components of the charge multipoles are present. Consequently, the results of the model Hamiltonian calculation, as we discuss below, have important implications for all polar metals, beyond the specific example of doped PTO.
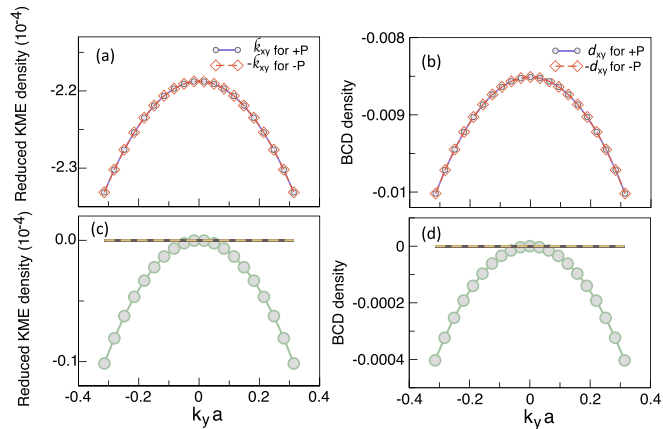
FIG. 7. Results of the tight-binding analysis. Computed variation (in circles) of (a) the reduced KME density component κ_{xy} and (b) the BCD density component d_{xy} around the Γ point along k_y for the $+P$ polarization. The same variation (in diamonds) for $-\kappa_{xy}$ and $-d_{xy}$ for the polarization $-P$ are also shown in (a), (b). The lines serve as a visual guide. The same variation of (c) κ_{xy}, (d) d_{xy} in the presence of inversion symmetry (black solid line), in absence of fourth-NN interorbital hopping parameters t^x and t^y (dashed brown line), and in absence of the first term (linear in $\vec{k}$) in Eq. (9) (green line with circles). The parameters used for the plots are listed in Table I, and $\alpha = 0.22$, $\beta = 0.02$, and $\gamma = -0.10$ (in units of 10^{-2} Ry) for $+P$ polarization.

3. Results and discussion

Now that we have correlated the individual terms of the Hamiltonian to the charge multipoles, we diagonalize the Hamiltonian $\mathcal{H}(\vec{k})$ in Eq. (6) for the realistic parameters listed in Table I, extracted using the NMTO downfolding technique [48,53]. We then use the computed eigenvalues ϵ_k^n and eigenfunctions u_k^n to obtain the k-space distribution of the Berry curvature and the orbital moment using Eq. (5) and the first term of Eq. (4), respectively, for the lowest energy band of the Hamiltonian in Eq. (6).

We then compute the BCD density $d_{ij}(\vec{k}) = \partial_{k_i}\Omega_j(\vec{k})$ and the reduced KME density $\kappa_{ij}(\vec{k}) = \partial_{k_i}m_j^{\text{orb}}(\vec{k})$ for $i, j = x, y$, the integrals of which over the occupied part of the BZ determine the magnitude of $\mathcal{D}_{ij}$ and $\tilde{\mathcal{K}}_{ij}$, respectively [see the second expressions in Eqs. (2) and (3)]. The computed densities show that they have the same sign ($+$ or $-$) over k space only if $i \neq j$ and hence when integrated over the occupied part of the BZ, only the xy and yx components of $\mathcal{D}$ and $\tilde{\mathcal{K}}$ have nonzero values. The variations of $d_{xy}(\vec{k})$ [$d_{yx}(\vec{k})$] and $\kappa_{xy}(\vec{k})$ [$\kappa_{yx}(\vec{k})$] along k_y (k_x) are shown in Fig. 7 (Fig. 10 of Appendix 3).

For the opposite polarization direction ($-P$), the parameters α, β, γ switch signs and, consequently, as shown in Figs. 7(a) and 7(b) (Fig. 10), the xy (yx) components of d and κ switch signs, keeping their magnitudes unaltered. In an $\mathcal{I}$-symmetric system, on the other hand, $\alpha = \beta = \gamma = 0$ and, consequently, we find that d_{ij}, κ_{ij} become zero as shown in Figs. 7(c) and 7(d), emphasizing the important role of $\mathcal{I}$ symmetry breaking. Our paper, therefore, identifies the interorbital hoppings, induced by the broken inversion symmetry, as the

microscopic origin of the KME and NHC responses in polar metals.

Further, to gain insight into the role of odd parity multipoles, we switch off the linear term in Eq. (9), which originates from the electric dipole moment. Interestingly, in this case, we find that while all considered components of d, κ still survive, their values reduce drastically by an order of magnitude. This suggests that the linear terms in k in Eq. (9), originating from the electric dipole moment, play an important role in determining the magnitudes of both these effects, although the importance of the electric octupole-driven k^3 terms cannot be ignored. Our findings are consistent with the multipole description of the KME response, proposed by Hayami *et al.* based on symmetry analysis [54]. Indeed, we find that the antisymmetric part of the KME response $\mathcal{K}_{ij}^-$ in PTO can be described by the existence of an electric dipole moment component, $\tilde{\mathcal{K}}_{ij}^- = \frac{1}{2}(\mathcal{K}_{ij} - \mathcal{K}_{ji}) = \varepsilon_{ijk}p_k$. It is important to point out here that the KME, although universal to all polar metals, can also occur in noncentrosymmetric but nonpolar systems, e.g., chiral materials, in which case other multipoles such as the monopole of the electric toroidal dipole moment will dictate the symmetric part (with the trace) of the KME response [54].

We further note that the fourth-NN [see Fig. 6(b)], interorbital ($d_{xy} - d_{xz}$ and $d_{xy} - d_{yz}$) hopping integrals, t^x and t^y, induced by the broken $\mathcal{I}$ symmetry, are the key ingredients for both effects. While both hopping integrals contribute to the parameters α and β, β is solely determined by t^x and t^y, while α has additional contributions. As a result, in the absence of these hoppings, β and the effective hopping, t_{eff}^8, in $\mathcal{H}_{\text{inv}}$ vanish. In this case of $t^x = t^y = 0$, we find that the components of both d and κ also vanish, as shown in Fig. 7 (see the dashed brown line), emphasizing the importance of the further neighbor interactions.

To understand why the fourth-NN hopping parameters are crucial, we first note that the nonzero β and t_{eff}^8 resulting from the fourth-NN hopping parameters appear in the third term of Eq. (9) and the off-diagonal elements h_{12} and h_{13} of Eq. (7), respectively. Interestingly, these are the only interorbital contributions in our minimal model that are also responsible for the band dispersion along the out-of-plane k_z direction. Since the inter-orbital hopping parameters drive the nonzero Berry curvature [55] and since the dispersion along k_z is crucial for the existence of the in-plane components of both orbital moment and Berry curvature [see Eqs. (4) and (5)], we see that both quantities vanish in the absence of fourth-NN hopping. This, in turn, also leads to an absence of xy and yx components of d and κ, explaining the crucial role of the fourth-NN hopping integrals in driving the KME and NHE in doped PTO.

IV. SUMMARY AND OUTLOOK

To summarize, taking the example of doped PTO, we have shown that both KME and the NHE are universal to all polar metals and can be used for a complete characterization of this class of materials. Our paper paves the way for the broad applicability of these two effects in polar metals, in general, going beyond their earlier investigation in topological systems [14,16,18,56]. Our detailed TB analysis reveals the

importance of the broken-symmetry-induced interorbital hopping parameters, correlated to the odd-parity charge multipoles, in mediating these effects. In particular, we have identified the broken-inversion-induced fourth-NN interorbital hopping parameters as being essential in driving these effects in doped PTO.

It is crucial to emphasize that both KME and NHC are present in a material as long as the polar distortion persists in the presence of itinerant charge carriers, defining the polar metal phase. However, beyond a certain doping concentration, the polar distortion in doped PTO is suppressed and, in this doping regime, the system is no longer in the polar metal phase. Consequently, both the NHC and KME also disappear. In essence, the KME and NHC are inherent to the polar metal phase, whether it is present intrinsically in the system or introduced by doping ferroelectric insulators.

Before concluding, here we briefly discuss possible routes to detecting the two effects. The second-order NHE in polar metals can be detected by measuring the second harmonic current $J_{2\omega}$ at a frequency 2ω for an applied ac electric field $\vec{E}$ of frequency ω [20]:

$$\vec{j}_{2\omega} = \frac{e^3\tau}{2(1+i\omega\tau)}\vec{E}_\omega \times (\vec{p} \times \vec{E}_\omega).$$ (11)

Here $\vec{p}$ is the direction of the electric dipole moment, which is along $\hat{z}$ for doped PTO. This suggests that for $\vec{E}$ along $\hat{z}$ (i.e., with polar angle $\theta = 0$), the Hall current vanishes, as we also found from our explicit calculations discussed above. Furthermore, for a general form of the field, $\vec{E} = Ee^{i\omega t}(\sin\theta\cos\phi, \sin\theta\sin\phi, \cos\theta)$, it is also easy to see from Eq. (11) that the Hall current does not depend on the azimuthal angle ϕ made by $\vec{E}$ with $\hat{x}$ for an in-plane $\vec{E}$ (i.e., $\theta = \pi/2$). This means that rotation of $\vec{E}$ within the x-y plane will leave the Hall current invariant.

The current-induced magnetization in the KME should be detectable using the magneto-optical Kerr effect. The computed reduced KME response is about an order of magnitude larger than that reported in Te [16]. In doped PTO, the generated magnetization is dominated by the orbital moment for a reasonable doping concentration [see the inset of Fig. 1(c)] and has a magnitude of $1.8 \times 10^{-4}\mu_B$/atom at the experimentally observed maximum doping concentration ($n_{x=0.12} = 1.9 \times 10^{21}$ cm^{-3}) up to which the system retains the ferroelectricity, and for an applied field of 10^5 V/m and a typical relaxation time constant $\tau \simeq 1$ ps [18]. For the same applied field, the computed total (spin plus orbital) magnetization is $\sim 1.0 \times 10^{-3}\mu_B$ per unit cell, which is comparable to the magnetization of the Rashba system Bi/Ag(111), the (001) surface of the topological insulator α-Sn, and the Weyl semimetal TaAs [18] and, hence, likely to be discernible in measurements.

In the present paper, we considered a rigid band approximation to describe the doped PTO case. While we expect this to provide a good description of the NHE and KME for the small doping concentration achievable in the measurements, future work should investigate computationally how electron doping affects the electronic structure of PTO. The dominance of the orbital magnetization in the KME response of doped PTO that emerges from our work, opens the door for the

application of polar metals in orbitronics with the additional advantage of switchable orbital texture by reversal of the electric polarization. We hope that our paper will motivate both theoretical and experimental work in these directions in the near future.

APPENDIX

1. Symmetry analysis of the *k*-space orbital moment and Berry curvature

Both the *k*-resolved contribution to the orbital magnetization $\vec{\mathcal{M}}^{\text{orb}}(\vec{k})$ (also, the Bloch orbital moment $\vec{m}^{\text{orb}}$) and $\vec{\Omega}(\vec{k})$ follow the same symmetry relations: Under spatial inversion $\mathcal{I}$ symmetry, both remain invariant, with $\vec{\mathcal{M}}^{\text{orb}}(\vec{k}) \xrightarrow{\mathcal{I}} \vec{\mathcal{M}}^{\text{orb}}(-\vec{k})$, whereas under time-reversal ($\mathcal{T}$) symmetry they switch signs, $\vec{\mathcal{M}}^{\text{orb}}(\vec{k}) \xrightarrow{\mathcal{T}} -\vec{\mathcal{M}}^{\text{orb}}(-\vec{k})$ [similarly for $\vec{\Omega}(\vec{k})$]. Hence, for a nonzero $\vec{\mathcal{M}}^{\text{orb}}(\vec{k})$ [$\vec{\Omega}(\vec{k})$], either of these two symmetries must be broken. In the present case, the broken $\mathcal{I}$ symmetry leads to nonzero values of $\vec{\mathcal{M}}^{\text{orb}}(\vec{k})$ and $\vec{\Omega}(\vec{k})$. Figure 8 depicts the *y* components of the *k*-resolved contribution to the orbital magnetization in Eq. (4) and the Berry curvature in Eq. (5) for small electron doping concentration. We note that since $\mathcal{T}$ symmetry is preserved, $\vec{\mathcal{M}}^{\text{orb}}$ ($\vec{\Omega}$) at $+\vec{k}$ has the opposite sign to that at $-\vec{k}$ and, as a result, the sum of $\vec{\mathcal{M}}^{\text{orb}}(\vec{k})$ [$\vec{\Omega}(\vec{k})$] over the occupied part of the Brillouin zone (BZ) is zero, consistent with the overall nonmagnetic behavior of PTO.

The key features of the computed distributions in Figs. 5 and 8 are the following. First, $\mathcal{M}_x^{\text{orb}}$ (and, hence, m_x^{orb}) and Ω_x are equal and opposite at $\pm k_y$, while they have the same sign at $\pm k_x$, consistent with the σ_v mirror symmetries [see Fig. 9(a)]
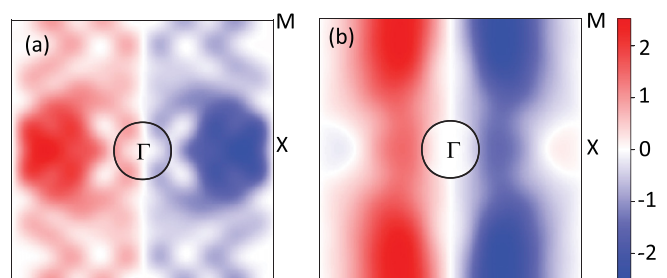

FIG. 8. Computed *k*-space distributions of (a) $\mathcal{M}_y^{\text{orb}}$ (in units of eV/Å^2) in Eq. (4) and (b) Ω_y (in units of Å^2) in Eq. (5) in PTO for the same doped electron density as in Fig. 5.
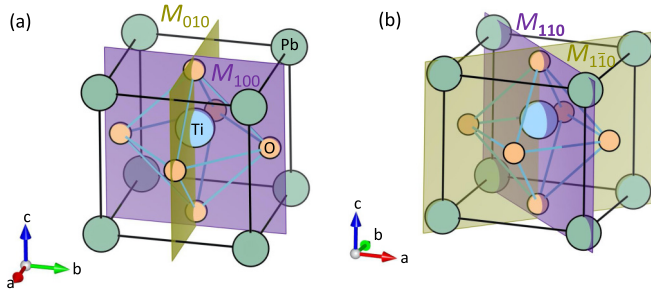
FIG. 9. (a) Vertical (σ_v) and (b) diagonal (σ_d) mirror planes in PTO.

that dictate

$$\mathcal{M}_x^{\text{orb}}(k_x, k_y, k_z) \xrightarrow{M_{100}} \mathcal{M}_x^{\text{orb}}(-k_x, k_y, k_z)$$

$$\text{and } \mathcal{M}_x^{\text{orb}}(k_x, k_y, k_z) \xrightarrow{M_{010}} -\mathcal{M}_x^{\text{orb}}(k_x, -k_y, k_z). \quad (A1)$$

In contrast, $\mathcal{M}_y^{\text{orb}}$ (m_y^{orb}) and Ω_y are equal and opposite at $\pm k_x$, while having the same sign at $\pm k_y$ due to the same σ_v symmetries, that is,

$$\mathcal{M}_y^{\text{orb}}(k_x, k_y, k_z) \xrightarrow{M_{100}} -\mathcal{M}_y^{\text{orb}}(-k_x, k_y, k_z)$$

$$\text{and } \mathcal{M}_y^{\text{orb}}(k_x, k_y, k_z) \xrightarrow{M_{010}} \mathcal{M}_y^{\text{orb}}(k_x, -k_y, k_z). \quad (A2)$$

Furthermore, the x and y components of $\vec{\mathcal{M}}^{\text{orb}}(\vec{k})$ [$\vec{m}^{\text{orb}}(\vec{k})$] and $\vec{\Omega}(\vec{k})$ are related to each other by the mirror $M_{1\bar{1}0}$ symmetry [see Fig. 9(b)], viz. $\mathcal{M}_x^{\text{orb}}(k_x, k_y, k_z) \xrightarrow{M_{1\bar{1}0}} -\mathcal{M}_y^{\text{orb}}(k_y, k_x, k_z)$. Moreover, since the velocity operator transforms as $(v_x, v_y, v_z) \xrightarrow{M_{1\bar{1}0}} (v_y, v_x, v_z)$ under the mirror $M_{1\bar{1}0}$ symmetry, Eq. (2) [Eq. (3)] leads to the constraint $\tilde{\mathcal{K}}_{xy} = -\tilde{\mathcal{K}}_{yx}$ [$\mathcal{D}_{xy} = -\mathcal{D}_{yx}$], in agreement with our results in Fig. 1(c) [Fig. 1(d)].

2. Derivation of the KME response

The BZ integral of Eq. (4) (the k-resolved contribution to the orbital magnetization) gives the net orbital magnetization

$$\vec{\mathcal{M}}^{\text{orb}} = \sum_n \int \frac{d^3k}{(2\pi)^3} f_{nk} \vec{\mathcal{M}}^{n,\text{orb}}(\vec{k})$$

$$= \sum_n \int \frac{d^3k}{(2\pi)^3} f_{nk} \left(\frac{e}{2\hbar} \text{Im}\langle \nabla_k u_k^n | \times [\mathcal{H}(\vec{k}) - \epsilon_k^n] | \nabla_k u_k^n \rangle \right.$$

$$\left. + \frac{e}{\hbar} \text{Im}\langle \nabla_k u_k^n | \times [\epsilon_k^n - \epsilon_F] | \nabla_k u_k^n \rangle \right)$$

$$= \sum_n \int \frac{d^3k}{(2\pi)^3} f_{nk} \left(\vec{m}^{n,\text{orb}}(\vec{k}) + [\epsilon_k^n - \epsilon_F] \frac{e}{\hbar} \vec{\Omega}_{n,k} \right). \quad (A3)$$

Here, $\vec{m}^{n,\text{orb}}(\vec{k})$ and $\vec{\Omega}_{n,k}$ are the Bloch orbital moment and the Berry curvature, respectively. In the presence of an electric field $\mathcal{E}_i$ along $\hat{i}$ in a metal, within the Boltzmann approximation, the nonequilibrium Fermi distribution function is

given by

$$f_{nk} = f_{nk}^0 - \frac{e}{\hbar} \mathcal{E}_i \tau v_{ni} \left(\frac{df_{nk}^0}{d\epsilon} \right) \bigg|_{\epsilon = \epsilon_k^n}. \quad (A4)$$

Here f_{nk}^0 is the equilibrium Fermi distribution function. Substituting Eq. (A4) in Eq. (A3), we get the magnetization induced by the current. Because of the time-reversal symmetry in equilibrium, the positive and negative regions of the orbital moment cancel each other to give rise to zero net orbital magnetization. Therefore, f_{nk}^0 does not contribute, and consequently we get

$$\vec{\mathcal{M}}^{\text{orb}} = -\frac{e\mathcal{E}_i \tau}{\hbar} \sum_n \int \frac{d^3k}{(2\pi)^3} \left(\vec{m}^{n,\text{orb}}(\vec{k}) + [\epsilon_k^n - \epsilon_F] \frac{e}{\hbar} \vec{\Omega}_{n,k} \right)$$

$$\times v_{ni} \left(\frac{df_{nk}^0}{d\epsilon} \right) \bigg|_{\epsilon = \epsilon_k^n}. \quad (A5)$$

Now, in the $T \to 0$ limit, $\frac{\partial f^0}{\partial \epsilon_k^n} = -\delta(\epsilon_k^n - \epsilon_F)$, and hence the second term in the above equation does not contribute, which gives

$$\vec{\mathcal{M}}^{\text{orb}} = -\frac{e}{\hbar} \mathcal{E}_i \tau \sum_n \int \frac{d^3k}{(2\pi)^3} \vec{m}^{n,\text{orb}}(\vec{k}) v_{ni} \left(\frac{df_{nk}^0}{d\epsilon} \right) \bigg|_{\epsilon = \epsilon_k^n}$$

$$= \frac{e}{\hbar} \mathcal{E}_i \tau \sum_n \int \frac{d^3k}{(2\pi)^3} f_{nk}^0 [\partial_{k_i} \vec{m}^{n,\text{orb}}(\vec{k})]. \quad (A6)$$

Comparing the above equation with $\mathcal{M}_j = \mathcal{K}_{ij} \mathcal{E}_i$ gives the expression for the KME
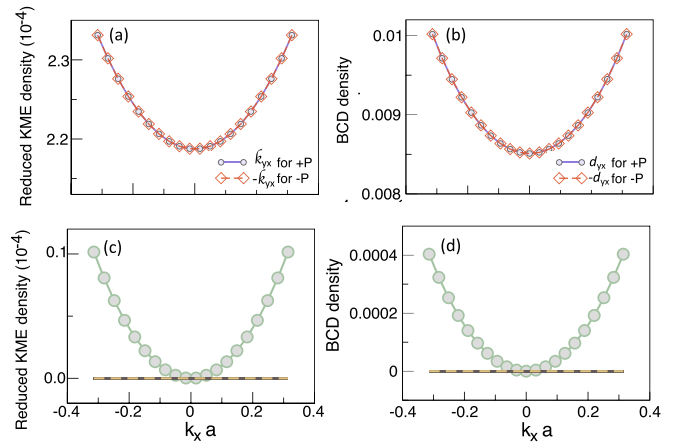

FIG. 10. Computed variation (in circles) of (a) the reduced KME density component κ_{yx}, and (b) the BCD density component d_{yx} around the Γ point along k_x for the $+P$ polarization. The same variation (indicated in diamonds) for $-\kappa_{yx}$ and $-d_{yx}$ for the polarization $-P$ are also shown in (a), (b). The lines are for a visual guide. The same variation of (c) κ_{yx} and (d) d_{yx} in the presence of inversion symmetry (black solid line), in absence of fourth-NN interorbital hopping parameters t^x and t^y (dashed brown line), and in absence of the first term (linear in $\vec{k}$) in Eq. (9) (green line with circles). The parameters used are the same as in Fig. 7.

response:

$$\mathcal{K}_{ij} = -\frac{e}{\hbar}\tau \sum_n \int \frac{d^3k}{(2\pi)^3} m_j^{n,\mathrm{orb}}(\vec{k}) v_{ni}\left(\frac{df_{nk}^0}{d\epsilon}\right)\Bigg|_{\epsilon=\epsilon_k^n}$$

$$= \frac{e}{\hbar}\tau \sum_n \int \frac{d^3k}{(2\pi)^3} f_{nk}^0 \big[\partial_{k_i} m_j^{n,\mathrm{orb}}(\vec{k})\big]. \qquad (A7)$$

3. Momentum space variation of κ_{yx} and d_{yx} as obtained from the model calculations

Figure 10 depicts the variation of the reduced KME density component κ_{yx} and the BCD density component d_{yx} along k_y as obtained from the model calculation, discussed in Sec. III D.

[1] P. W. Anderson and E. I. Blount, Symmetry considerations on martensitic transformations: "Ferroelectric" metals? Phys. Rev. Lett. **14**, 217 (1965).

[2] Y. Shi, Y. Guo, X. Wang, A. J. Princep, D. Khalyavin, P. Manuel, Y. Michiue, A. Sato, K. Tsuda, S. Yu, M. Arai, Y. Shirako, M. Akaogi, N. Wang, K. Yamaura, and A. T. Boothroyd, A ferroelectric-like structural transition in a metal, Nat. Mater. **12**, 1024 (2013).

[3] Z. Fei, W. Zhao, T. A. Palomaki, B. Sun, M. K. Miller, Z. Zhao, J. Yan, X. Xu, and D. H. Cobden, Ferroelectric switching of a two-dimensional metal, Nature (London) **560**, 336 (2018).

[4] P. Sharma, F.-X. Xiang, D.-F. Shao, D. Zhang, E. Y. Tsymbal, A. R. Hamilton, and J. Seidel, A room-temperature ferroelectric semimetal, Sci. Adv. **5**, eaax5080 (2019).

[5] W. X. Zhou and A. Ariando, Review on ferroelectric/polar metals, Jpn. J. Appl. Phys. **59**, SI0802 (2020).

[6] S. Bhowal and N. A. Spaldin, Polar metals: Principles and prospects, Annu. Rev. Mater. Res. **53**, 53 (2023).

[7] D. Hickox-Young, D. Puggioni, and J. M. Rondinelli, Polar metals taxonomy for materials classification and discovery, Phys. Rev. Mater. **7**, 010301 (2023).

[8] X. Zhang, C. Xiao, Z. Zhang, L. Dong, H. Pan, C. Cao, S. A. Yang, S.-H. Wei, and Y. Lu, Origin of versatile polarization state in CuInP$_2$S$_6$, Phys. Rev. B **108**, L161406 (2023).

[9] Q. Ma, S.-Y. Xu, H. Shen, D. MacNeill, V. Fatemi, T.-R. Chang, A. M. Mier Valdivia, S. Wu, Z. Du, C.-H. Hsu, S. Fang, Q. D. Gibson, K. Watanabe, T. Taniguchi, R. J. Cava, E. Kaxiras, H.-Z. Lu, H. Lin, L. Fu, N. Gedik *et al.*, Observation of the nonlinear Hall effect under time-reversal-symmetric conditions, Nature (London) **565**, 337 (2019).

[10] K. Kang, T. Li, E. Sohn, J. Shan, and K. F. Mak, Nonlinear anomalous Hall effect in few-layer WTe$_2$, Nat. Mater. **18**, 324 (2019).

[11] R.-C. Xiao, D.-F. Shao, W. Huang, and H. Jiang, Electrical detection of ferroelectriclike metals through the nonlinear Hall effect, Phys. Rev. B **102**, 024109 (2020).

[12] L. S. Levitov, Yu. V. Nazarov, and G. M. Éliashberg, Magnetoelectric effects in conductors with mirror isomer symmetry, Zh. Eksp. Teor. Fiz. **88**, 229 (1985) [Sov. Phys. JETP **61**, 133 (1985)].

[13] T. Yoda, T. Yokoyama, and S. Murakami, Current-induced orbital and spin magnetizations in crystals with helical structure, Sci. Rep. **5**, 12024 (2015).

[14] S. Zhong, J. E. Moore, and I. Souza, Gyrotropic magnetic effect and the magnetic moment on the Fermi surface, Phys. Rev. Lett. **116**, 077201 (2016).

[15] C. Şahin, J. Rou, J. Ma, and D. A. Pesin, Pancharatnam-berry phase and kinetic magnetoelectric effect in trigonal tellurium, Phys. Rev. B **97**, 205206 (2018).

[16] S. S. Tsirkin, P. A. Puente, and I. Souza, Gyrotropic effects in trigonal tellurium studied from first principles, Phys. Rev. B **97**, 035158 (2018).

[17] I. E. Dzyaloshinskiĭ, On the magneto-electrical effect in antiferromagnets, J. Expt. Theor. Phys. (U.S.S.R.) **37**, 881 (1959) [Sov. Phys. JETP **10**, 628 (1960)].

[18] A. Johansson, J. Henk, and I. Mertig, Edelstein effect in Weyl semimetals, Phys. Rev. B **97**, 085417 (2018).

[19] K. Limtragool and K. Pasanai, Large enhancement of Edelstein effect in Weyl semimetals from Fermi-arc surface states, Phys. E: Low Dimens. Syst. Nanostruct. **135**, 114983 (2022).

[20] I. Sodemann and L. Fu, Quantum nonlinear Hall effect induced by Berry curvature dipole in time-reversal invariant materials, Phys. Rev. Lett. **115**, 216806 (2015).

[21] D. G. Ovalle, A. Pezo, and A. Manchon, Influence of the surface states on the nonlinear Hall effect in Weyl semimetals, Phys. Rev. B **106**, 214435 (2022).

[22] J. Son, K.-H. Kim, Y. H. Ahn, H.-W. Lee, and J. Lee, Strain engineering of the Berry curvature dipole and valley magnetization in monolayer MoS$_2$, Phys. Rev. Lett. **123**, 036806 (2019).

[23] M. Huang, Z. Wu, J. Hu, X. Cai, E. Li, X. An, X. Feng, Z. Ye, N. Lin, K. T. Law, and N. Wang, Giant nonlinear Hall effect in twisted bilayer WSe2, Natl. Sci. Rev. **10**, nwac232 (2023).

[24] R.-C. Xiao, D.-F. Shao, Z.-Q. Zhang, and H. Jiang, Twodimensional metals for piezoelectriclike devices based on Berry-curvature dipole, Phys. Rev. Appl. **13**, 044014 (2020).

[25] H. Isobe, S.-Y. Xu, and L. Fu, High-frequency rectification via chiral Bloch electrons, Sci. Adv. **6**, eaay2497 (2020).

[26] Y. Zhang and L. Fu, Terahertz detection based on nonlinear Hall effect without magnetic field, Proc. Natl. Acad. Sci. **118**, e2100736118 (2021).

[27] The gyrotropic point groups are those crystal point groups that allow the presence of both polar ($\vec{P}$) and axial ($\vec{L}$) vector components transforming according to equivalent representations of the point group. The 18 gyrotropic point groups, therefore, allow for a second-rank tensor, connecting physical quantities P_i and L_j, that describes physical effects such as natural optical activity.

[28] W.-Y. He and K. T. Law, Magnetoelectric effects in gyrotropic superconductors, Phys. Rev. Res. **2**, 012073(R) (2020).

[29] S. Bhowal, S. P. Collins, and N. A. Spaldin, Hidden *k*-space magnetoelectric multipoles in nonmagnetic ferroelectrics, Phys. Rev. Lett. **128**, 116402 (2022).

[30] R. J. Nelmes and W. F. Kuhs, The crystal structure of tetragonal PbTiO$_3$ at room temperature and at 700 K, Solid State Commun. **54**, 721 (1985).

[31] J.-X. Gu, K.-J. Jin, C. Ma, Q.-H. Zhang, L. Gu, C. Ge, J.-S. Wang, C. Wang, H.-Z. Guo, and G.-Z. Yang, Coexistence of

polar distortion and metallicity in $PbTi_{1-x}Nb_xO_3$, Phys. Rev. B **96**, 165206 (2017).

[32] T. Iijima, H. Näfe, and F. Aldinger, Ferroelectric properties of Al and Nb doped $PbTiO_3$ thin films prepared by chemical solution deposition process, Integr. Ferroelectr. **30**, 9 (2000).

[33] P. Giannozzi, S. Baroni, N. Bonini, M. Calandra, R. Car, C. Cavazzoni, D. Ceresoli, G. L. Chiarotti, M. Cococcioni, I. Dabo, A. D. Corso, S. de Gironcoli, S. Fabris, G. Fratesi, R. Gebauer, U. Gerstmann, C. Gougoussis, A. Kokalj, M. Lazzeri, L. Martin-Samos *et al.*, QUANTUM ESPRESSO: A modular and open-source software project for quantum simulations of materials, J. Phys.: Condens. Matter **21**, 395502 (2009).

[34] N. Marzari and D. Vanderbilt, Maximally localized generalized Wannier functions for composite energy bands, Phys. Rev. B **56**, 12847 (1997).

[35] I. Souza, N. Marzari, and D. Vanderbilt, Maximally localized Wannier functions for entangled energy bands, Phys. Rev. B **65**, 035109 (2001).

[36] A. A. Mostofi, J. R. Yates, G. Pizzi, Y.-S. Lee, I. Souza, D. Vanderbilt, and N. Marzari, An updated version of wannier90: A tool for obtaining maximally-localised Wannier functions, Comput. Phys. Commun. **185**, 2309 (2014).

[37] W.-Y. He, D. Goldhaber-Gordon, and K. T. Law, Giant orbital magnetoelectric effect and current-induced magnetization switching in twisted bilayer graphene, Nat. Commun. **11**, 1650 (2020).

[38] S. Bhowal and S. Satpathy, Orbital gyrotropic magnetoelectric effect and its strain engineering in monolayer NbX_2, Phys. Rev. B **102**, 201403(R) (2020).

[39] D. Hara, M. S. Bahramy, and S. Murakami, Current-induced orbital magnetization in systems without inversion symmetry, Phys. Rev. B **102**, 184404 (2020).

[40] E. Rashba, Properties of semiconductors with an extremum loop. I. Cyclotron and combinational resonance in a magnetic field perpendicular to the plane of the loop, Sov. Phys.-Solid State **2**, 1109 (1960).

[41] D. Xiao, J. Shi, and Q. Niu, Berry phase correction to electron density of states in solids, Phys. Rev. Lett. **95**, 137204 (2005).

[42] T. Thonhauser, D. Ceresoli, D. Vanderbilt, and R. Resta, Orbital magnetization in periodic insulators, Phys. Rev. Lett. **95**, 137205 (2005).

[43] D. Ceresoli, T. Thonhauser, D. Vanderbilt, and R. Resta, Orbital magnetization in crystalline solids: Multi-band insulators, Chern insulators, and metals, Phys. Rev. B **74**, 024408 (2006).

[44] J. Shi, G. Vignale, D. Xiao, and Q. Niu, Quantum theory of orbital magnetization and its generalization to interacting systems, Phys. Rev. Lett. **99**, 197202 (2007).

[45] M. G. Lopez, D. Vanderbilt, T. Thonhauser, and I. Souza, Wannier-based calculation of the orbital magnetization in crystals, Phys. Rev. B **85**, 014435 (2012).

[46] D. Xiao, M.-C. Chang, and Q. Niu, Berry phase effects on electronic properties, Rev. Mod. Phys. **82**, 1959 (2010).

[47] D. J. Thouless, M. Kohmoto, M. P. Nightingale, and M. den Nijs, Quantized Hall conductance in a two-dimensional periodic potential, Phys. Rev. Lett. **49**, 405 (1982).

[48] O. K. Andersen and T. Saha-Dasgupta, Muffin-tin orbitals of arbitrary order, Phys. Rev. B **62**, R16219 (2000).

[49] D. Go, J.-P. Hanke, P. M. Buhl, F. Freimuth, G. Bihlmayer, H.-W. Lee, Y. Mokrousov, and S. Blügel, Toward surface orbitronics: Giant orbital magnetism from the orbital Rashba effect at the surface of *sp*-metals, Sci. Rep. **7**, 46742 (2017).

[50] D. Go, D. Jo, T. Gao, K. Ando, S. Blügel, H.-W. Lee, and Y. Mokrousov, Orbital Rashba effect in a surface-oxidized Cu film, Phys. Rev. B **103**, L121113 (2021).

[51] R. Arras, J. Gosteau, H. J. Zhao, C. Paillard, Y. Yang, and L. Bellaiche, Rashba-like spin-orbit and strain effects in tetragonal $PbTiO_3$, Phys. Rev. B **100**, 174415 (2019).

[52] N. A. Spaldin, M. Fechner, E. Bousquet, A. Balatsky, and L. Nordström, Monopole-based formalism for the diagonal magnetoelectric response, Phys. Rev. B **88**, 094429 (2013).

[53] Per-Olov Löwdin, A note on the quantum-mechanical perturbation theory, J. Chem. Phys. **19**, 1396 (1951).

[54] S. Hayami, M. Yatsushiro, Y. Yanagi, and H. Kusunose, Classification of atomic-scale multipoles under crystallographic point groups and application to linear response tensors, Phys. Rev. B **98**, 165110 (2018).

[55] S. Bhowal and S. Satpathy, Electric field tuning of the anomalous Hall effect at oxide interfaces, npj Comput. Mater. **5**, 61 (2019).

[56] S. Roy and A. Narayan, Non-linear Hall effect in multi-Weyl semimetals, J. Phys.: Condens. Matter **34**, 385301 (2022).